Arch. Metall. Mater. **70** (2025), 1, 199-209

DOI: https://doi.org/10.24425/amm.2025.152534

S. AHMAD[1], M.F. OMAR[1,2*], E.M. MAHDI[3], K.A.A. HALIM[1,2], S.Z. ABD RAHIM[2], H. MD AKIL[4], N. NOSBI[5], N. YUDASARI[6], M.H. HASSAN[7], S.S. MD SALEH[1,2], M.B.H. OTHMAN[8]

MOLECULAR INTERACTIONS BETWEEN POLYURETHANE AND UiO-66 IN POLYMER-MOF NANOCOMPOSITES: MICROSTRUCTURAL AND MECHANICAL EFFECTS

The demand for polymer-based nanocomposite-reinforced nanoporous materials is becoming essential in sustainable development studies. Integrating nanoporous materials such as Metal-Organic Frameworks (MOFs) in polymer matrices is essential for developing sustainable advanced materials. Combining MOFs and polymer matrices can produce a hybrid material with improved mechanical strength and stability relative to its constituents. This study aims to elucidate the effect of synthesised UiO-66 nanoparticles in a polyurethane (PU) matrix on the subsequent hybrid materials' microstructural and mechanical properties. UiO-66 nanoparticles were synthesised at 120°C, 130°C, and 140°C. The nanoparticles and subsequent nanocomposite were characterised using X-ray Diffraction (XRD), Fourier Transform Infrared Spectroscopy (FT-IR), Brunauer-Emmett-Teller (BET), and Field Emission-Secondary Electron Microscopy (FE-SEM). The experimental findings indicate that the UiO-66 nanoparticles synthesised at 130°C exhibited a highly desirable crystal structure and effective adsorption properties, and the nanoparticles synthesised at this temperature were then used to reinforce PU, forming a polymer-MOF nanocomposite. The mechanical properties of the resulting nanocomposite were determined using tensile and nanoindentation tests. The UiO-66 nanoparticles were incorporated into PU matrices at various weight percentages (10 wt.%, 20 wt.%, 30 wt.%, and 40 wt.%) via the solution casting technique. The results indicated that 30 wt.% UiO-66 in the polymer nanocomposite exhibits the best mechanical properties, and loading the polymer nanocomposite beyond 30 wt.% is more likely to result in nanoparticle agglomeration and brittle behaviours.

Keywords: Metal-organic frameworks (MOFs); UiO-66; polymer nanocomposites; polyurethane (PU)

1. Introduction

Polymer composites are an active area of research and development due to their wide range of applications across various industries. Polymer composites result from a combination of two or more distinct components, where polymers act as reinforcing matrices, and the particles act as filler materials, culminating in a hybrid material with better properties than its respective constituents. One of the primary advantages of polymer composites is their high strength-to-weight ratio, which makes them ideal for use in structural applications where weight reduction is critical. Also, these materials offer excellent resistance to corrosion and wear, rendering them suitable for use in harsh environments. Polymer composites also exhibit excellent thermal and electrical conductivities, making them useful in various electronic and thermal management applications. These advantages prompted many researchers to investigate methods for realising better dispersion and alignment of nanomaterials within polymer matrices. There is also a rapid study of microporous materials as potential reinforcements to improve the mechanical properties of composites. This study focuses on microporous material metal-organic frameworks (MOFs). MOFs are reported to possess significantly higher surface area and pore volumes, enhancing interfacial bonding between matrices and support and improving strength and stiffness as they feature interconnected pores with less than 2 nm in diameter [1]. This results in a vast surface area, typically ~300-2000 m^2/g [2]. MOFs are among the most well-known microporous materials due to the possibility of modifying

[1] UNIVERSITI MALAYSIA PERLIS, FACULTY OF CHEMICAL ENGINEERING AND TECHNOLOGY PERLIS, MALAYSIA
[2] UNIVERSITI MALAYSIA PERLIS, GEOPOLYMER AND GREEN TECHNOLOGY, CENTRE OF EXCELLENT (CEGEOGTECH PERLIS, MALAYSIA
[3] MALAYSIA NUCLEAR AGENCY, MATERIALS TECHNOLOGY GROUP, INDUSTRIAL TECHNOLOGY DIVISION, 43000, KAJANG, SELANGOR, MALAYSIA
[4] UNIVERSITI SAINS MALAYSIA, SCHOOL OF MATERIALS AND MINERAL RESOURCES ENGINEERING, ENGINEERING CAMPUS 14300 NIBONG TEBAL, PULAU PINANG, MALAYSIA
[5] UNIVERSITI TEKNOLOGI PETRONAS, DEPARTMENT OF MECHANICAL ENGINEERING, CENTRE FOR CORROSION RESEARCH (CCR), INSTITUTE OF CONTAMINANT MANAGEMENT FOR OIL AND GAS (ICM), 32610, PERAK, MALAYSIA
[6] RESEARCH CENTER FOR PHOTONICS, NATIONAL RESEARCH AND INNOVATION AGENCY, KAWASAN PUSPIPTEK GD. 442 TANGERANG SELATAN, INDONESIA, 15314
[7] UNIVERSITI SAINS MALAYSIA, SCHOOL OF MECHANICAL ENGINEERING, ENGINEERING CAMPUS, 14300 NIBONG TEBAL, PULAU PINANG, MALAYSIA
[8] UNIVERSITI SAINS MALAYSIA, SCHOOL OF CHEMICAL SCIENCES, GELUGOR, 11800, PULAU PINANG MALAYSIA

* Coressponding author: firdausomar@unimap.edu.my

their advantageous features, most notably their selectivities and capacities [3]. MOFs are commonly used as catalysts for flue gas filtration and adsorbent.

MOFs are crystalline, highly porous, and used to store, disperse, and trap gases. Metal ions and organic molecules known as "linkers" comprise their structure [4], per Fig. 1. Selecting suitable metallic cores and linkers for the MOFs can positively impact their selectivities and capacities. MOFs consist of metal ions linked to rigid organic molecules to form porous one-, two-, or three-dimensional structures. These metals provide coordination environments of diverse geometries. Due to metal complexes' typical liability, coordination connections between metal ions and organic linkers can be reversibly formed [5], which makes them malleable during polymerisation, resulting in highly structured framework structures (or the provision of such networks) [6]. MOFs have many advantages over conventional microporous materials, especially in gas sorption and storage. Due to their potential to produce materials that selectively absorb certain gases into bespoke pockets within structures, applications like gas storage and separation, liquid separation and purification, electrochemical energy storage, catalysis, and sensing utilises MOFs [7].

UiO-66 (Universitetet i Oslo) is a MOF made up of $[Zr_6O_4(OH)_4]$ clusters with 1,4-benzodicarboxylic acid struts [8]. The structure of the inorganic brick and the nature of the chemical bonds it forms with the linker are the main factors affecting the MOFs' stability. Many MOFs exhibited weak thermal, chemical, and mechanical stability, which limited their use in large-scale industrial applications. However, UiO-66 (and isoreticular UiO-67 and UiO-68) is a zirconium-based MOF (UiO-66) with a very high surface area and remarkable thermal stability. Much research has been conducted on UiO-66 for the adsorption of small molecules due to its exceptional thermal, chemical, and mechanical durability. Fig. 2 shows UiO-66's structure [9].

Knowledge of the synthesis process and properties of UiO-66 in a solution containing a high concentration of precursors is crucial. The properties of porous crystal materials are dictated by their morphology, which is challenging to control. UiO-66 synthesis methods can tailor crystal morphology by manipulating the chemical reaction route, crystal nucleation, crystal nucleation, and growth rates. However, the connecting carboxylate remains unaltered during synthesis, indicating that the inner Zr_6-cluster is reversible in its dryness and hydration.

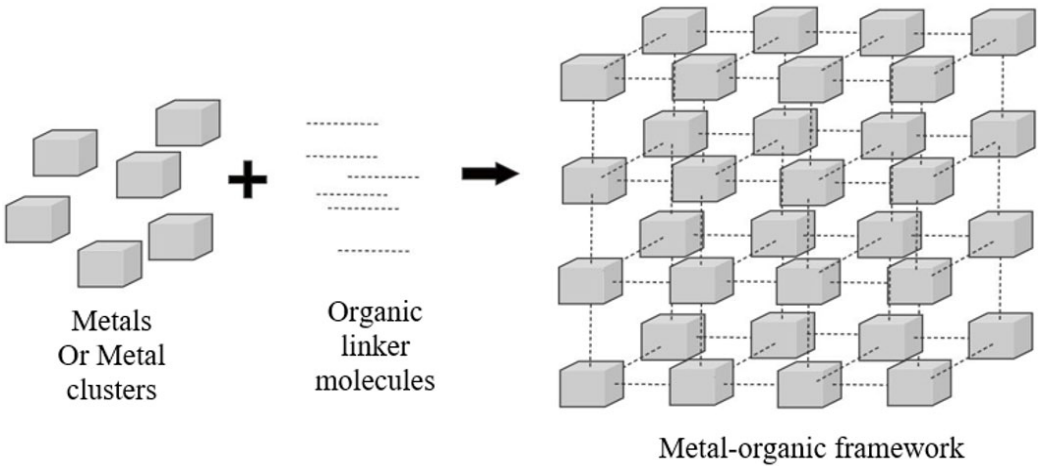

Fig. 1. Schematic structure of MOFs

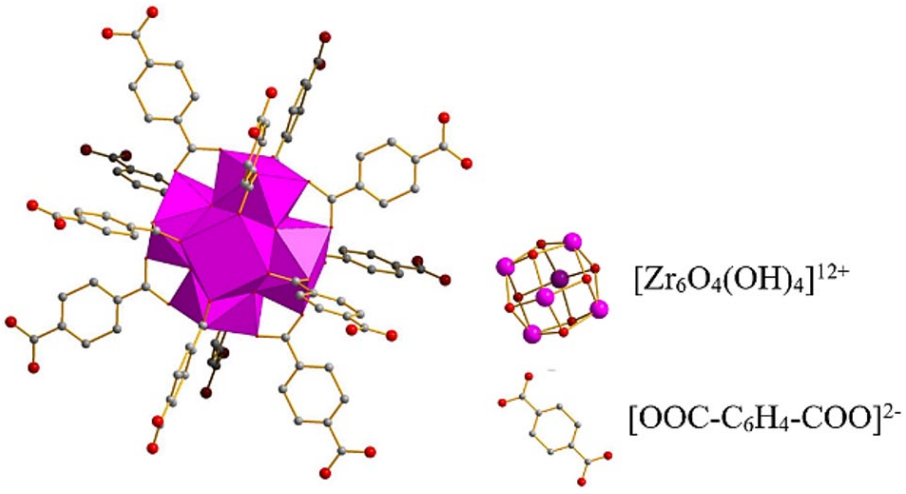

Fig. 2. The structure of UiO-66, made up of $Zr_6O_4(OH)_4$ clusters and 1,4-benzenedicarboxylic acid (BDC) linkers [9]

Kandiah et al. reported that the UiO-66 has a Langmuir surface area of ~1187 m^2/g and excellent air stability of up to 500°C [10].

Despite numerous reports on the fabrication of UiO-66--reinforced polymer in the literature, not many focussed on the influence of nanoparticle loading on the subsequent properties of UiO-66-reinforced polyurethane (PU) nanocomposite. This work compared the effectiveness of UiO-66 nanoparticle loadings towards the microstructural and mechanical properties of synthesised UiO-66-reinforced PU. X-ray Diffraction (XRD), Fourier Transform Infrared Spectroscopy (FT-IR), Brunauer-Emmett-Teller (BET) analysis and Field Emission-Secondary Electron Microscopy (FE-SEM) analysis were used to characterise the structural and morphological properties of both UiO-66 nanoparticles and the PU/UiO-66 polymer nanocomposites. The mechanical properties of the nanoparticles and polymer nanocomposites were determined using the tensile and nanoindentation tests.

2. Materials and methods

2.1. Materials

Zirconium (IV) propoxide solution, acetic acid, and terephthalic acid were purchased from Sigma Aldrich Sdn. Bhd., while tetrahydrofuran (THF) and n,n-dimethylformamide (DMF) solutions were purchased from Merck Sdn. Bhd.

2.2. Synthesis of UiO-66 nanoparticles

UiO-66 nanoparticles were prepared using the previously reported room temperature synthesis method [11]. 70 µL of a Zirconium Propoxide solution was added to 1-propanol (0.158 mmol), 7 mL DMF, and 4 mL acetic acid. The subsequent solution will be heated to ~130°C for two hours till it becomes a yellowish solution (clear to yellow). After two hours, it was cooled to room temperature. Upon cooling, the BDC linker (1,4-benzenedicarboxylate) was added to the solution in stages to form the UiO-66. The solution was sonicated for 30 s and stirred for 18 h at a fixed temperature of 25°C. Then, the UiO-66 solutions were centrifuged and washed using DMF, and the solvent was exchanged with THF for storage. The procedure was repeated at temperatures 120°C and 140°C.

2.3. Fabrication of UiO-66/PU nanocomposites

UiO-66/PU nanocomposites were fabricated using the solution casting method [12]. Polyurethane (PU) polymer solution was prepared by dissolving ~1 g of Poly [4,4'-methylenebis (phenyl isocyanate)-alt-1,4-butanediol/di (propylene glycol)/ polycaprolactone] beads in tetrahydrofuran (THF) for a total of 24-48 hours until the pellets are visually determined to have completely dissolved in the THF-laden solution. The previously synthesised UiO-66 nanoparticles, dispersed as colloids, were added to the PU solution, corresponding to the wt.% Eq. (1):

$$\mathrm{UiO-66\ wt.\%} = \frac{m(\mathrm{UiO-66})}{m(\mathrm{UiO-66}) + m(\mathrm{PU})} \times 100\% \qquad (1)$$

where $m_{\mathrm{UiO\text{-}66}}$ is the weight of the UiO-66 nanoparticles dispersed in THF, while m_{PU} is the weight of the PU beads dissolved in THF. This produced four distinct solutions of polymer nanocomposites with varied UiO-66 nanoparticles' loading: 10, 20, 30 and 40 wt.%. Song et al. [13] confirmed that applying this colloidal solution mixing approach may significantly reduce the possibility of nanoparticles' agglomeration, otherwise witnessed in polymer nanocomposites produced by the re-dispersion of dried UiO-66 nanoparticles. After 24 h of drying, the polymer nanocomposites were detached from the glass plate and stored for subsequent studies.

2.4. Characterisation methods

2.4.1. Structural analysis using X-ray Diffractometer (XRD)

The powder sample was placed on Polymethyl methacrylate (PMMA) Perspex and the XRD magazine sample holder. Its crystallinity was obtained using an X-ray diffractometer (XRD, Bruker AXS D8 Advance) with Cu-kα radiation source (λ = 1.54 Å) at an accelerating voltage of 40 kV. The diffractogram was recorded in the $\varphi = 2\theta$ angle ranging from 5°-50° with a step interval size of 0.04, and data was collected at a scan rate of 2°/min.

2.4.2. Chemical bonds analysis using Fourier Transform Infrared Spectroscopy (FT-IR)

The Fourier-transform infrared spectroscopy (FTIR) instrument was used to determine bond types for UiO-66 nanoparticles and PU/UiO-66 polymer nanocomposites. Test samples were sectioned (~5 mm^2) from larger specimens and analysed in the FTIR apparatus. The FTIR spectra consist of vibration peaks representing specific bond types. Due to the speculation that the organic ligands within the MOF nanoparticles form weak interactions with the polymer matrix (PU), vibrational peaks representing both constituents are expected to appear in the spectra. The results garnered from the FTIR analyses are also qualitative and correlated to those from the XRD analysis.

2.4.3. Morphological analysis using Field Emission-Scanning Electron Microscopy (FE-SEM)

The morphology of UiO-66 nanoparticles and PU/UiO-66 polymer nanocomposites was examined using the Field

Emission-Scanning Electron Microscope (FE-SEM). The powder samples were dispersed and mounted on a stub using adhesives. Each sample was coated with platinum using a sputter coater for 30 s prior to imaging at 20 kV under a high vacuum. The sample was heated in the oven at 80°C for 30 min to eliminate the moisture/water before fixing it on the sample stub.

2.5. Mechanical properties analysis

2.5.1. Tensile test

The (quantitative) quasi-static properties of the UiO-66/PU nanocomposites were determined using the tensile test. The stress-strain (σ-ε) plots of the PU/UiO-66 polymer nanocomposites were generated using data collected from the Instron Universal Testing Machine (UTM) equipped with a 100-N load cell (ASTM D882). The samples, measuring 100 mm × 15 mm, were clamped to the rig and subjected to a tensile load applied at a displacement rate of ~10 mm/min until failure.

2.5.2. Nanoindentation test

A nanoindenter with a Berkovich three-sided pyramid diamond tip was used to determine Young's modulus (E) and indentation hardness (H) of the PU/UiO-66 polymer nanocomposites. A rectangular grid of 20 indentations was produced for each probed sample (three polymer nanocomposites tested per wt.%).

3. Result and discussion

3.1. Characterisation of UiO-66 particles

3.1.1. Morphology analysis

Fig. 3(a)-(c) shows the structures of the synthesised UiO-66 at various temperatures. It can be seen in Figs. 3(a) and 3(b) that the UiO-66 nanoparticles are cubic in configuration, while Fig. 3(c) shows UiO-66 in spherical configuration. These morphologies agree with [14-16]. It can be observed that the grain of the freshly prepared sample emerges from the crystalline crystal with sharp edges, with both having an average particle size of ~0.5-1.5 µm. Due to the vigorous contact reaction with increasing temperatures, the UiO-66 nanoparticles' colour changes from yellowish-white to pale yellow [16]. Fig. 3(a)-(c) demonstrates how the UiO-66 nanoparticles' shapes change at higher temperatures, shrinking and becoming less angular [17]. The morphological characteristics of the UiO-66 nanoparticles agree with that reported by Destefano et al. [11], where they posited that increasing temperature significantly decreased the density of defects and indirectly resulted in smaller particles.

Fig. 4(a)-(c) shows the XRD pattern of the UiO-66 nanoparticles at 120°C, 130°C and 140°C, respectively. The diffraction peaks are present at 5° and 20°. All peaks in the obtained XRD analysis of specimens (a), (b), and (c) agreed with the JCPDS card No. 96-451-2073, which confirms the formation of UiO-66. UiO-66 nanoparticles synthesised at 130°C shows the highest intensity (crystallinity) formed at 7.38°, 8.50° and 12.04°

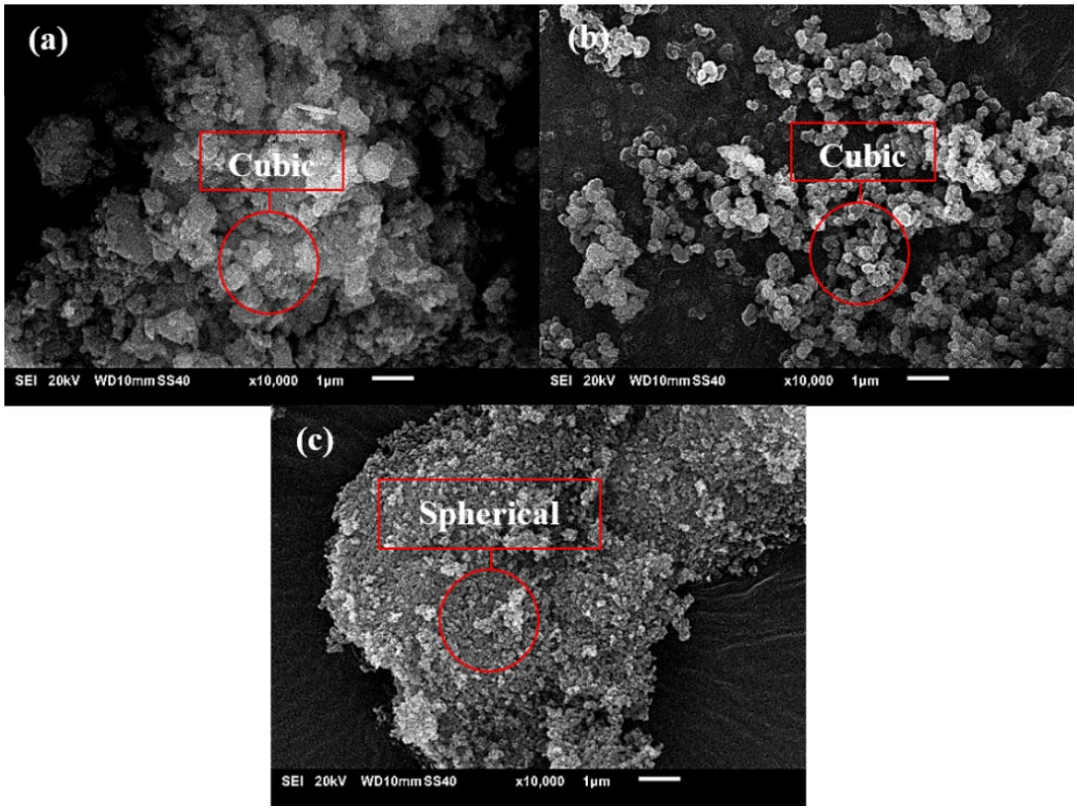

Fig. 3. FE-SEM images of synthesised UiO-66 nanoparticles at temperatures: (a) 120°C, (b) 130°C, and (c) 140°C

(5°-15°) corresponding to the (111), (020) and (022) planes of Zr. Although it was believed thatb increasing the temperature would decrease the defect density due to the increased lability of intermediate linkers, a high synthesis temperature could also lead to the decomposition of the UiO-66 main crystalline network [18]. The results suggest that, for this synthesis procedure, the optimum synthesis temperature for UiO-66 nanoparticles is 130°C.

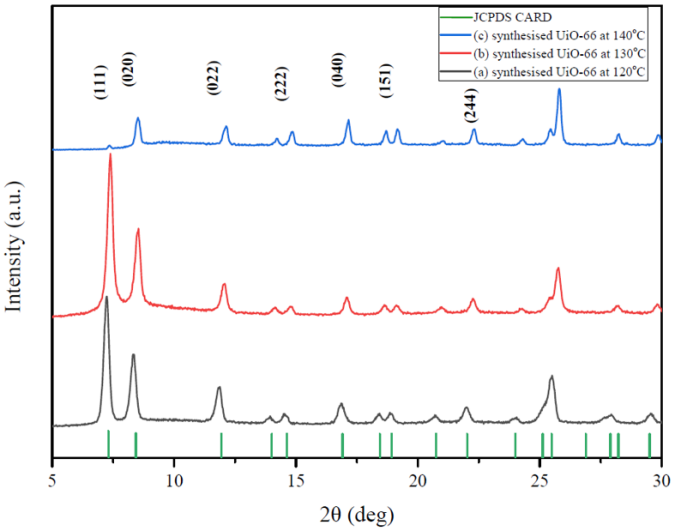

Fig. 4. Simulated and observed the XRD pattern of UiO-66 nanoparticles at temperatures (a) 120°C, (b) 130°C, and (c) 140°C

Fig. 5 shows the N_2 adsorption/desorption of synthesised UiO-66 particles at 120°C, 130°C, and 140°C. The plot shows that the values of BET surface area of the synthesised UiO-66 are (a) 590.132, (b) 784.214, and (c) 710.522 m^2g^{-1}, respectively. Again, synthesised UiO-66 at 130°C recorded the highest BET surface area. This phenomenon can be attributed to the decrement of defect density with increasing synthesis temperature [11]. It is speculated that defect sites, as illustrated in Fig. 6, whether resulting from missing linkers or clusters, render the framework space more accessible [18]. However, high temperatures could destroy the main framework structure, indirectly decreasing the surface area of MOFs nanoparticles, as seen in specimen (c).

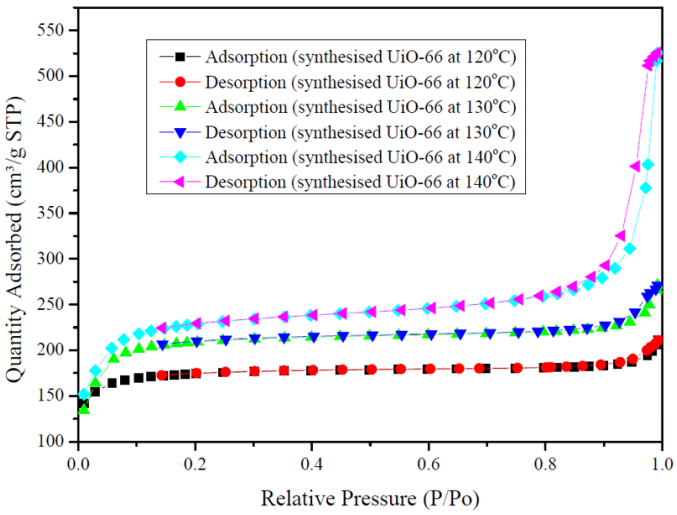

Fig. 5. N_2 adsorption/desorption isotherms of UiO-66 (a)-(b)

3.1.2. FT-IR analysis

Fig. 7 shows the FTIR spectra of synthesised UiO-66 nanoparticles at 120°C, 130°C, and 140°C, respectively. The exhibited characteristic peaks of UiO-66 show a similar pattern to the one reported previously [11]. At the spectra of ~481 cm^{-1}, the formation of UiO-66 was Zr-O, indicating the vibration of the substance at that point. The intense peaks at ~1656 cm^{-1} were confirmed to be C = O stretching modes from carboxylic acids. The broad spectrum of ~3100-3500 cm^{-1} shows that the organic linker combined with the metal is fully utilised as there is no other slope of the vibration of O-H stretching [19]. The patterned peaks show excellent agreement with Han et al. [20]. The FTIR results confirmed the formation of UiO-66 nanoparticles for all synthesis temperatures. Overall, it is convenient to posit that the optimum synthesis temperature (excellent crystal structure and good adsorption capability) for the synthesised UiO-66 nanoparticles is 130°C and, therefore, this temperature will be further utilised during PU/UiO-66 polymer nanocomposite fabrication.

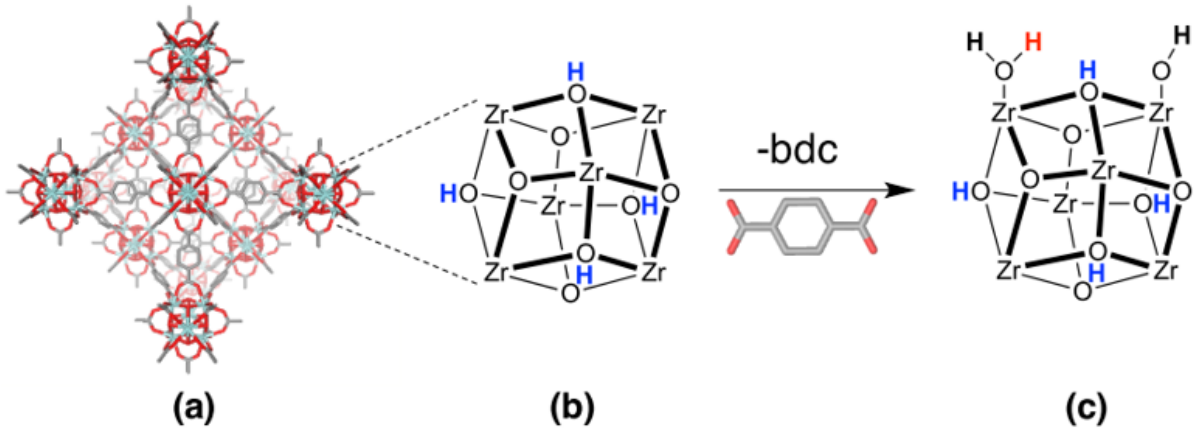

Fig. 6. (a) Structure of UiO-66 (b) an ideal 12-connected SBU and (c) a defective (11-connected) SBU with –OH/–OH_2 capping ligands. The three types of protons in (c) are marked blue, red and black for the μ3–OH, terminal –OH_2 and terminal –OH protons, respectively [11]

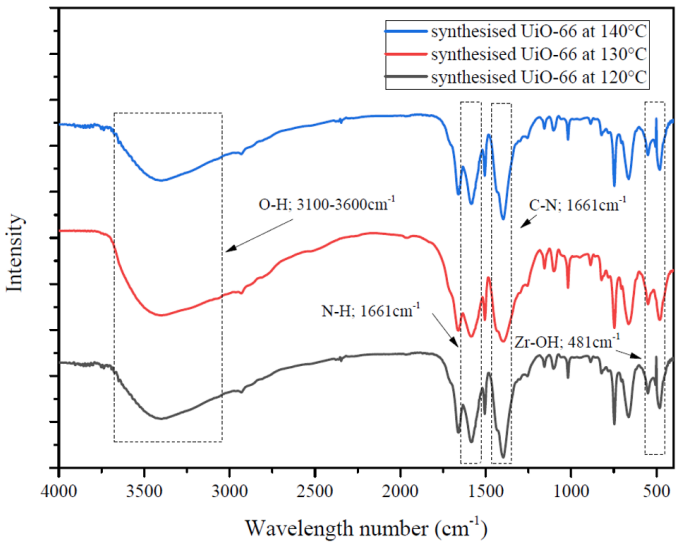

Fig. 7. FT-IR spectrum of UiO-66 at various temperatures

3.2. Characterisation of UiO-66/PU nanocomposite

3.2.1. Structural analysis using X-ray Diffractometer (XRD)

Fig. 8 shows the XRD patterns of neat PU, synthesised UiO-66 nanoparticles, and various particle loadings of UiO-66--reinforced PU (PU/UiO-66). The sharp peaks exhibited by UiO-66 nanoparticles confirm its excellent crystallinity. Generally, Fig. 8 shows that UiO-66 agrees with the JCPDS card No. 96-451-2073, confirming the formation of UiO-66. The synthesised UiO-66 nanoparticles at 130°C show the highest peak formed at 7.38°, 8.50° and 12.04° (5°-15°) corresponding to the (111), (020) and (022) planes of Zr, respectively. Neat PU exhibits the same patterns reported by Dias et al. [21]. The various particle loadings PU/UiO-66/PU overlap, with the increasing particle loading inhibiting the amorphous pattern of PU and showing a sharp peak as UiO-66 dominate the polymer chain of the nanocomposite.

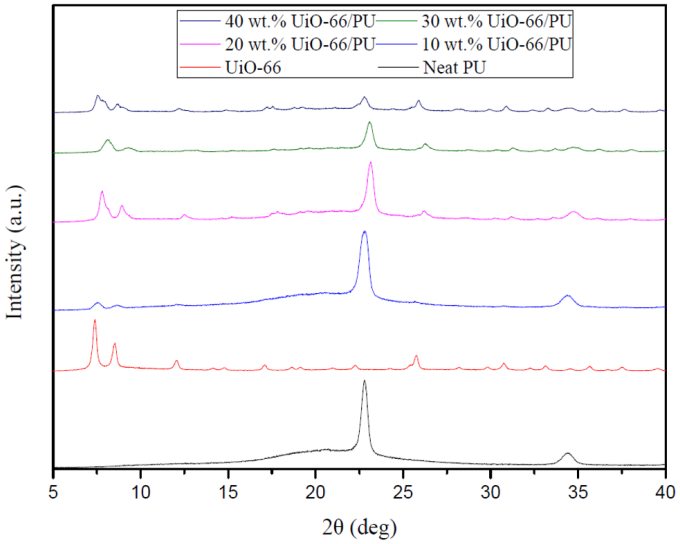

Fig. 8. XRD pattern of Neat PU, UiO-66 and various particle loading of PU/UiO-66

3.2.2. FT-IR analysis

Fig. 9 shows the FT-IR spectrums of UiO-66, PU, and PU/UiO-66 polymer nanocomposites. For the PU FT-IR spectrum, the absorption band at ~3323 cm^{-1} corresponds to N-H stretching, while the absorption band at ~1734 cm^{-1} is associated with C = O stretching, corresponding to the PU spectrum reported in a previous study [22]. The increasing particle loading inhibits the amorphous pattern of PU and shows UiO-66 dominating the polymer chain of the nanocomposite. It also shows that the intensity of all UiO-66 characteristic peaks increases with increasing particle loading up to 30 wt.%.

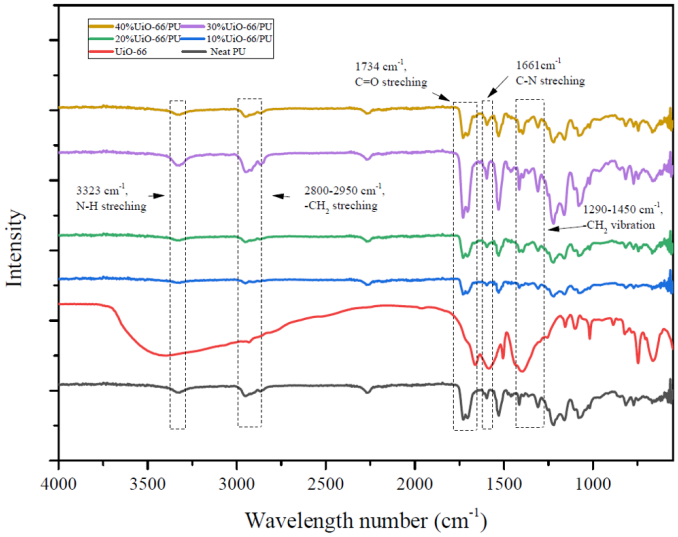

Fig. 9. FTIR spectrum of Neat PU, UiO-66, and PU/UiO-66 polymer nanocomposite with various particle loading samples in the wavelength number range of ~550-4000 cm^{-1}

3.3. Mechanical properties

3.3.1. Tensile properties

The stress-strain plots of PU/UiO-66 polymer nanocomposites with various particle loading (10 wt.%, 20 wt.%, 30 wt.%, and 40 wt.%) are shown in Fig. 10. It can be seen that the 30 wt.% of particle loading has the highest flow of stress values. This can be attributed to the molecular chain of the nanocomposite being significant up to 30 wt.%, after which it begins to immobilise the internal structures; UiO-66 dominated the composite chain, and poorly bonded particles resulted in stress transfer at PU/UiO-66 interface being inefficient [23,24]. Fig. 11 shows the ductility, fracture energy, yield strength, and ultimate tensile strength of PU/UiO-66. The ductility and fracture energy of PU/UiO-66 decreases as the particle loading increases, and it improves the composite's stiffness. Increased loadings of MOF nanoparticles

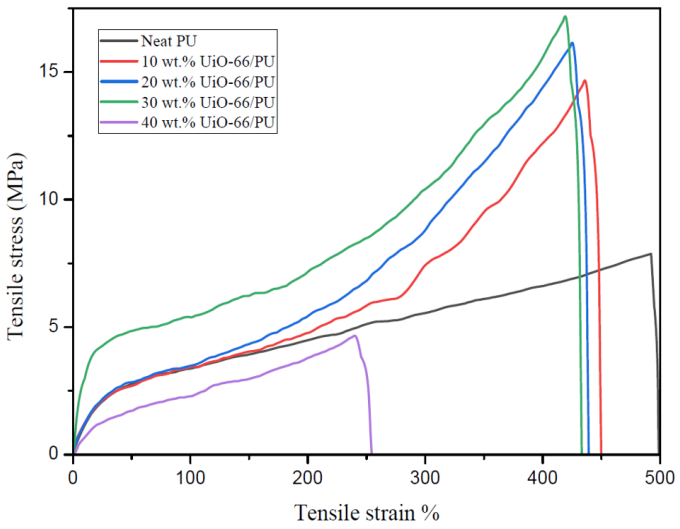

Fig. 10. Stress-strain curves of UiO-66/PU nanocomposites with different particle loading (10 wt.%, 20 wt.%, 30 wt.%, and 40 wt.%)

resulted in smaller amounts of PU polymeric chains per unit volume in the nanocomposites, where the polymeric chains loosely associated with the MOF nanoparticles undergo reduction at a typical level for PU [25]. The ultimate tensile strength decreases with increasing particle loading due to the stiffness, making the material more brittle and easier to fracture. The yield strength of 30 wt.%, PU/UiO-66, recorded the highest value of 3.55 MPa; thus, it has the maximum tensile stress that can withstand the deformation better than the rest of the particle loading. >30 wt.% particle loading, the yield strength decreases. The yield strength increases could be due to the filler's strengthening effect due to the fine dispersion in the polymer matrix [25]. The same goes for the ultimate tensile strength; the increasing particle loading eventually decreases the strength. The yield strength of PU/UiO-66 increases with increased particle loading up to 30 wt.%. The decreased hyperelasticity at 40 wt.% PU/UiO-66 indicates that the agglomeration of UiO-66 makes it brittle and stiffer [26]. The higher the particle loading, the higher the filler tends to agglomerate as it occupies the matrix. Also, nanoparticles have a higher tendency to agglomerate [27], and the agglomeration of filler tends to become a concentrated stress point and points of fracture due to uneven stress distribution between the matrix and filler. At lower particle loadings, agglomeration is minimal, and ductile behaviour predominates. Fig. 12 illustrates the nanocomposite deformation behaviour post-tensile test.

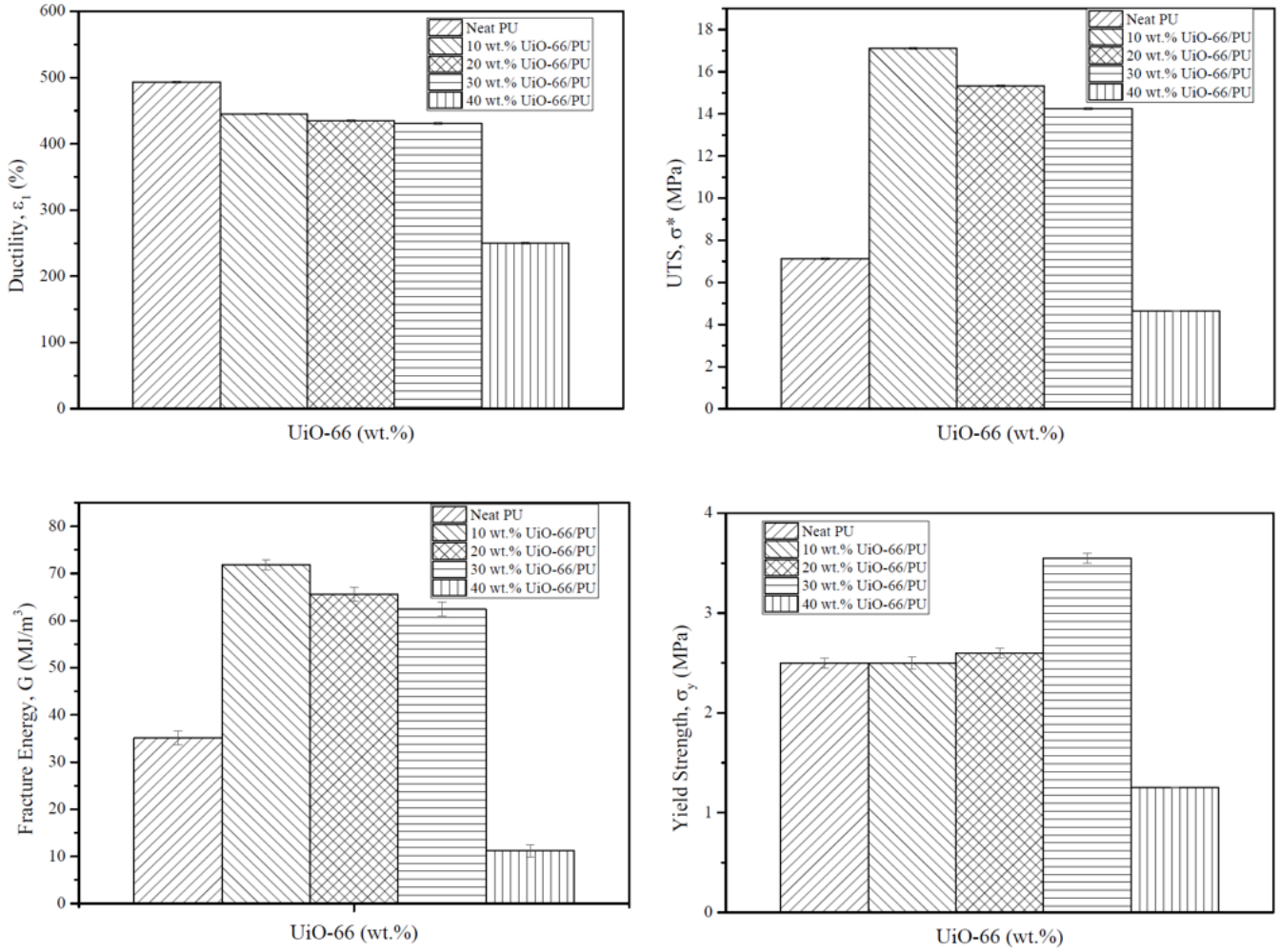

Fig. 11. The mechanical properties of UiO-66/PU nanocomposite derived from the stress-strain plots (Fig. 4), with (a) ductility (ef), (b) fracture energy (Gf), (c) ultimate tensile strength (σ^*), and (d) yield strength (σy). The calculated values averaged from three test coupons and the corresponding standard deviations for each sample on the error bars

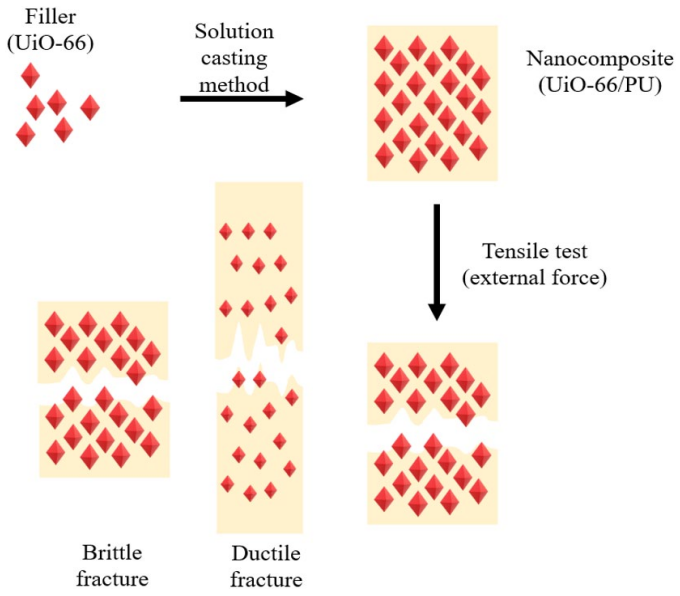

Fig. 12. Illustration of deformation behaviour of UiO-66-reinforced polyurethane

3.3.2. Nanoindentation behaviour

Fig. 13 shows the nanohardness (H) and Young's Modulus (E) of the PU/UiO-66 polymer nanocomposites. The highest nanohardness and E values of PU/UiO-66 are 40.8 MPa and 150 MPa at 40 wt% particle loading, respectively. Theoretically, H, as measured by the nanoindentation technique, is directly proportional to UiO-66 nanoparticle loading regardless of the particle dispersion state. It can be seen that the filler has significantly improved the hardness of the material as it is attributed to better rigidity and stiffness properties due to the incorporation of stiffer UiO-66 nanoparticles within the PU matrix, which efficiently hinders chain movement during deformation [25]. A comparable observation has been documented by Mahdi et al., who postulated that the observed increase in hardness values with higher particle loading could be attributed to the pinning and suspension effects induced by the UiO-66 nanoparticle [28].

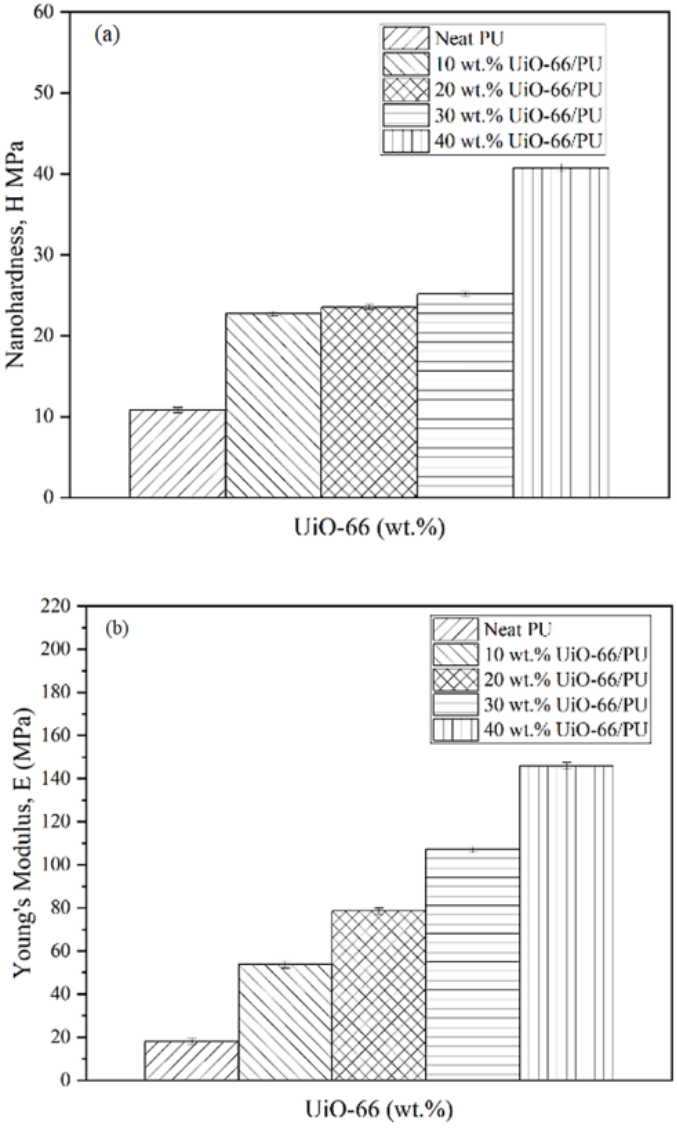

Fig. 13. Nanoindentation data: (a) Nanohardness (E), (b) Young's Modulus (H) reported for polyurethane and PU/UiO-66 nanocomposite. The reported results are the average of multiple indents (penetration depth of 2 mm) made on random points on the sample's surface to represent the samples' E and H properties as possible

3.4. Post-damage analysis

Post-damage analysis was performed to identify whether the MOF nanoparticles (UiO-66) and matrix (PU) are blended or remain as distinct, separate phases, the distribution of MOF particles throughout the matrix, and the preservation of the morphological features of the MOF particles encapsulated with the matrix. According to Shahid et al. [29], these factors are directly correlated to the performance of these composites, where it was mentioned that the agglomeration and uneven distribution of MOF particles within the matrix may result in decreased composite properties, especially in gas separation performance. Also, Mahdi et al. [30] stated that the separate phases of MOF particles and matrices within a composite resulted in compromised macro-mechanical properties. Understanding the nature of the interaction between MOF particles and their matrix will help us determine whether or not it is viable for its intended applications. Field Emission-Scanning Electron Microscopy (FE-SEM) was employed to analyse the fracture surfaces of nanocomposites in order to investigate the underlying mechanism responsible for their strengthening, as portrayed in Fig. 14. Based on the FE-SEM images, it can be seen that the PU/UiO-66 nanocomposite exhibits a rough surface and distinct "sea waves-like" features, per Fig. 14(b)-(e) [31]. In contrast to the smooth fracture surface typically observed in neat polyurethane (PU), the rougher surfaces observed in the nanocomposites exhibited enhanced energy absorption capabilities prior to tensile failure. This phenomenon may account for the significant improvements in tensile properties and the toughening and strengthening mechanisms observed in the polymer matrix upon incorporating the nanoparticles. Incorporating UiO-66 at 10

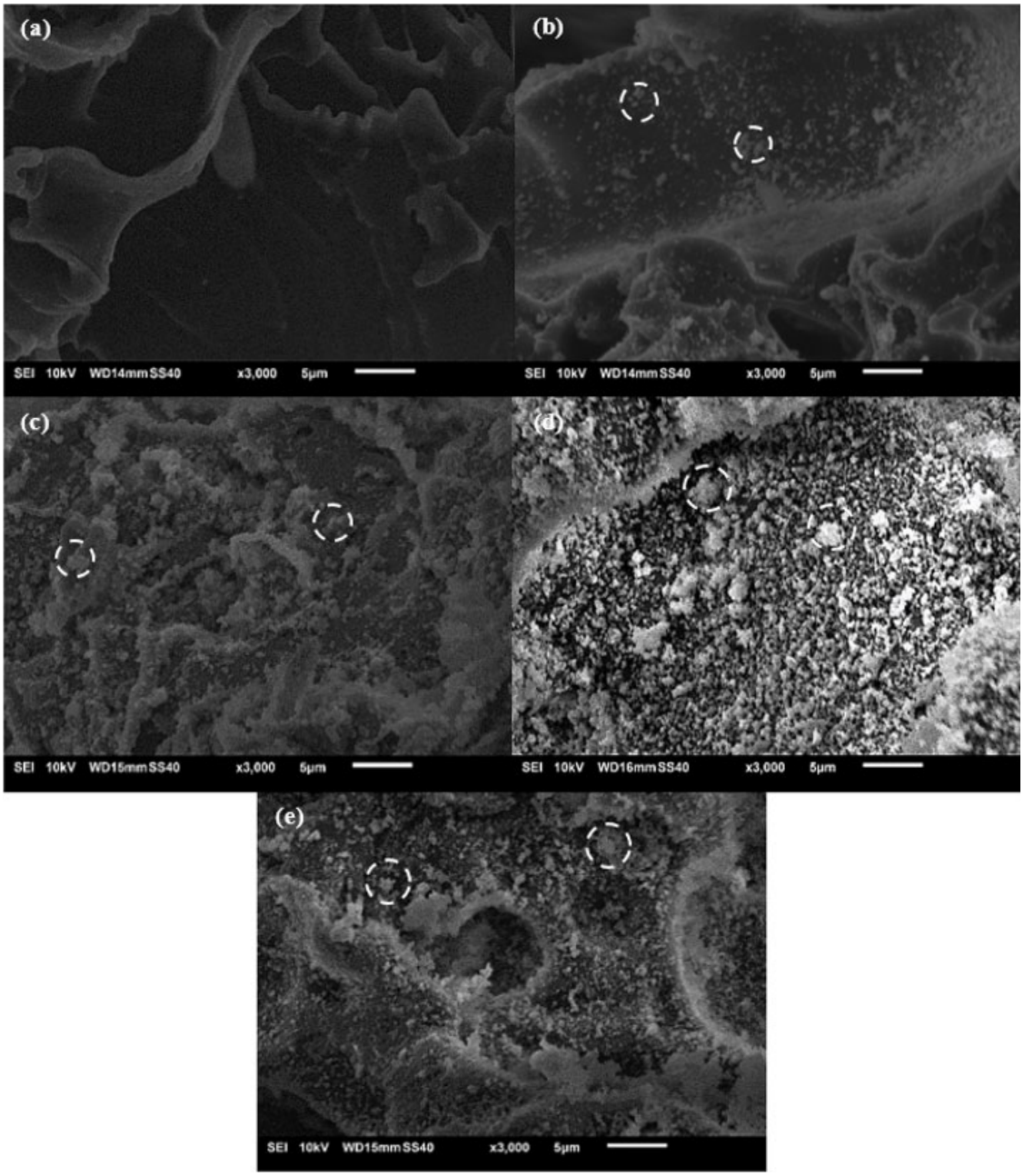

Fig. 14. Field Emission-Scanning Electron Microscopy (FE-SEM) micrographs showing the cross sections of UiO-66/Polyurethane nanocomposite membranes. (a) Polyurethane matrix, while (b)-(e) are composites containing UiO-66 nanoparticles loadings of 10, 20, 30 and 40 wt.%, respectively. The samples were fractured from tensile testing, exposing their cross-sectional area for high-resolution imaging. The white circles in the images indicate examples of encapsulated UiO-66 nanoparticles. Images were taken at ~3,000 magnification under 10 kV

and 20 wt.% in the polymer matrix results in a scalloped vein structure surrounding the MOF particles [32]. This observation suggests the presence of a robust interfacial interaction between the polymer and filler particles. The absence of any observed gaps between the polymer and filler particles, commonly known as the "sieve-in-a-cage" effect, was noted [32]. The augmentation of MOF loading to 30 wt.% resulted in a comparatively homogeneous dispersion of MOF particles, while the loading of 40 wt.% of UiO-66/PU led to the aggregation of particles [26]. Fig. 14(e) images reveal white metal-organic framework (MOF) particle aggregates. These aggregates are observed to induce cracking due to residual stress in the film, including nanoparticles within a polymer matrix, resulting in the enhancement of the stiffness of the nanocomposite. This is achieved through the mechanical interaction between the polymer chains and the nanoparticles. The extent to which stress is distributed between the polymer matrix and the nanoparticles is influenced by the interfacial area and the stiffness of the nanoparticles [26]. The stiffening efficiency quantifies the relationship between the properties of nanoparticles and their ability to enhance the stiffness of nanocomposites. Therefore, when the particle loading is increased to less than 30 wt.%, the interaction between UiO-66 and PU in PU/UiO-66 nanocomposites becomes notably influential.

4. Conclusion

The microstructural and mechanical effects on PU/UiO-66 nanocomposites were successfully investigated. From the results, the following conclusions can be drawn:

- The synthesised UiO-66 at temperatures of 120°C, 130°C, and 140°C were confirmed using X-Ray Diffraction, Field Emission-Scanning Electron Microscopy (FE-SEM), Brunauer-Emmett-Teller (BET) analysis, and Fourier Transform Infrared (FT-IR). From the data, the synthesised UiO-66 at 130°C show an excellent crystal structure and good adsorption. Thus, fabrication of the synthesised UiO-66 at 130°C reinforced PU was carried out;
- Results show that the UiO-66 nanoparticles had significantly affected the mechanical properties of the UiO-66/PU composites. Quantitatively, 30 wt.% of PU/UiO-66 nanocomposite reported the highest ultimate strength, stiffness and yield behaviour, while the 40 wt.% PU/UiO-66/PU nanocomposite reported the highest *H* and *E*;
- The mechanical contact and the interfacial characteristic between the UiO-66 nanoparticles and the PU polymer chains were successfully observed via post-damage analysis. It has been confirmed that the interaction between UiO-66 and PU in PU/UiO-66 nanocomposites becomes more significant when the particle loading increases up to 30 wt.% (optimum nanoparticle loading) before it starts to show decrements.

Acknowledgement

The author would like to acknowledge the Malaysian Ministry of Higher Education (MOHE), Fundamental Research Grant (FRGS) (Grant no.: FRGS/1/2020/TK0/UNIMAP/02/58) and Universiti Malaysia Perlis (incentive grant) for sponsoring and providing financial assistance for this research work.

REFERENCES

[1] P. Kumar, K. Vellingiri, K.H. Kim, R.J.C. Brown, M.J. Manos, Modern progress in metal-organic frameworks and their composites for diverse applications. Microporous and Mesoporous Material **253**, no. October, 251-265 (2017). DOI: https://doi.org/10.1016/j.micromeso.2017.07.003

[2] M. Alhamami, H. Doan, C.H. Cheng, A review on breathing behaviors of metal-organic-frameworks (MOFs) for gas adsorption. Materials (Basel) **7**, 4, 3198-3250 (2014). DOI: https://doi.org/10.3390/ma7043198

[3] Y. Zhang, X. Feng, S. Yuan, J. Zhou, B. Wang, Challenges and recent advances in MOF-polymer composite membranes for gas separation. Inorg. Chem. Front. **3**, 7, 896-909 (2016). DOI: https://doi.org/10.1039/c6qi00042h

[4] L. Zhang et al., Erratum: NH2-MIL-53(Al) Metal-Organic Framework as the Smart Platform for Simultaneous High-Performance Detection and Removal of Hg2+. (Inorg. Chem. **58**, 19 (12573-12581) (2019). (DOI: https://doi.org/10.1021/acs.inorgchem.9b01242)). Inorg. Chem. **59**, 14, 10375-10376 (2020). DOI: https://doi.org/10.1021/acs.inorgchem.0c01787

[5] M. Bonneau, C. Lavenn, P. Ginet, K.I. Otake, S. Kitagawa, Upscale synthesis of a binary pillared layered MOF for hydrocarbon gas storage and separation. Green Chem. **22**, 3, 718-724 (2020). DOI: https://doi.org/10.1039/c9gc03561c

[6] M. Ding, H.L. Jiang, Improving water stability of metal–organic frameworks by a general surface hydrophobic polymerization. CCS Chem. **3**, 8, 2740-2748 (2021). DOI: https://doi.org/10.31635/ccschem.020.202000515

[7] M.I.H. Mohideen et al., A Fine-Tuned MOF for Gas and Vapor Separation: A Multipurpose Adsorbent for Acid Gas Removal, Dehydration, and BTX Sieving. Chem. **3**, 5, 822-833 (2017). DOI: https://doi.org/10.1016/j.chempr.2017.09.002

[8] N. Liu, L. Shi, X. Meng, Tuning the adsorption properties of UiO-66 via acetic acid modulation. J. Chem. Sci. **131**, 6 (2019). DOI: https://doi.org/10.1007/s12039-019-1628-3

[9] W.I.R.S. Wissen, UiO-66: a case study metal-organic framework. pp. 2-46, 2016.

[10] M. Kandiah et al., Synthesis and stability of tagged UiO-66 Zr-MOFs. Chem. Mater. **22**, 24, 6632-6640 (2010). DOI: https://doi.org/10.1021/cm102601v

[11] M.R. DeStefano, T. Islamoglu, S.J. Garibay, J.T. Hupp, O.K. Farha, Room-Temperature Synthesis of UiO-66 and Thermal Modulation of Densities of Defect Sites. Chem. Mater. **29**, 3, 1357-1361 (2017). DOI: https://doi.org/10.1021/acs.chemmater.6b05115

[12] S. Samal, B. Svomova, M. Spasovová, O. Tyc, D. Vokoun, I. Stachiv, Physical, Thermal, and Mechanical Characterization of PMMA Foils Fabricated by Solution Casting. Appl. Sci. **13**, 2 (2023). DOI: https://doi.org/10.3390/app13021016

[13] Q. Song et al., Zeolitic imidazolate framework (ZIF-8) based polymer nanocomposite membranes for gas separation. Energy Environ. Sci. **5**, 8, 8359-8369 (2012). DOI: https://doi.org/10.1039/c2ee21996d

[14] T. Zhang et al., Rapid synthesis of UiO-66 by means of electrochemical cathode method with electrochemical detection of 2,4,6-TCP. Inorg. Chem. Commun. **111**, no. October 2019, 107671 (2020). DOI: https://doi.org/10.1016/j.inoche.2019.107671

[15] Y. Yin, Y. Wang, L. Meng, Uio-66 as nucleating agent on the crystallization behavior and properties of poly (Ethylene terephthalate). Polymers (Basel). **13**, 14, (2021). DOI: https://doi.org/10.3390/polym13142266

[16] F.J.H., Temperature dependence of the rate of reaction in thermal analysis The Arrhenius equation in condensed phase kinetics. J. Therm. Anal. **36**, 1579-1593 (1990).

[17] K.S. Lin, A.K. Adhikari, C.N. Ku, C.L. Chiang, H. Kuo, Synthesis and characterization of porous HKUST-1 metal organic frameworks for hydrogen storage. Int. J. Hydrogen Energy **37**, 18, 13865-13871 (2012). DOI: https://doi.org/10.1016/j.ijhydene.2012.04.105

[18] C.D. Malonzo et al., Thermal Stabilization of Metal-Organic Framework-Derived Single-Site Catalytic Clusters through Nanocasting. J. Am. Chem. Soc. **138**, 8, 2739-2748 (2016). DOI: https://doi.org/10.1021/jacs.5b12688

[19] I. Ardelean, S. Cora, FT-IR, Raman and UV-VIS spectroscopic studies of copper doped 3Bi 2O 3·B 2O 3 glass matix. J. Mater. Sci. Mater. Electron. **19**, 6, 584-588 (2008).
DOI: https://doi.org/10.1007/s10854-007-9393-3

[20] Y. Han et al., Facile synthesis of morphology and size-controlled zirconium metal-organic framework UiO-66: the role of hydrofluoric acid in crystallization. Cryst. Eng. Comm. **17**, 33, 6434-6440 (2015). DOI: https://doi.org/10.1039/c5ce00729a

[21] R.C.M. Dias, A.M. Góes, R. Serakides, E. Ayres, R.L. Oréfce, Porous biodegradable polyurethane nanocomposites: Preparation, characterization, and biocompatibility tests. Mater. Res. **13**, 2, 211-218 (2010).
DOI: https://doi.org/10.1590/S1516-14392010000200015

[22] A. Asefnejad, M. T. Khorasani, A. Behnamghader, B. Farsadzadeh, S. Bonakdar, Manufacturing of biodegradable polyurethane scaffolds based on polycaprolactone using a phase separation method: physical properties and in vitro assay. Int. J. Nanomedicine **6**, 2375-2384 (2011). DOI: https://doi.org/10.2147/ijn.s15586

[23] C. Li, J. Liu, K. Zhang, S. Zhang, Y. Lee, T. Li, Coating the Right Polymer: Achieving Ideal Metal–Organic Framework Particle Dispersibility in Polymer Matrixes Using a Coordinative Crosslinking Surface Modification Method. Angew. Chemie – Int. Ed. **60**, 25, 14138-14145 (2021).
DOI: https://doi.org/10.1002/anie.202104487

[24] S.Y. Fu, X.Q. Feng, B. Lauke, Y.W. Mai, Effects of particle size, particle/matrix interface adhesion and particle loading on mechanical properties of particulate-polymer composites. Compos. Part B Eng. **39**, 6, 933-961 (2008).
DOI: https://doi.org/10.1016/j.compositesb.2008.01.002

[25] C. Onuoha, O.O. Onyemaobi, C.N. Anyakwo, G.C. Onuegbu, Open Access Effect Of Filler Loading And Particle Size On The Mechanical Properties Of Periwinkle Shell-Filled Recycled Polypropylene. American Journal of Engineering Research (AJER) **6**, 4, 72-79 (2017).

[26] M.A. Ashraf, W. Peng, Y. Zare, K.Y. Rhee, Effects of Size and Aggregation/Agglomeration of Nanoparticles on the Interfacial/Interphase Properties and Tensile Strength of Polymer Nanocomposites. Nanoscale Res. Lett. **13**, (2018).
DOI: https://doi.org/10.1186/s11671-018-2624-0

[27] Y. Dahman, H. Javaheri, J. Chen, B.A.-C. Sulaiman, Chapter 5 – Nanoparticles. In Micro and Nano Technologies pp. 93-119 (2017).

[28] E.M. Mahdi, J.C. Tan, Dynamic molecular interactions between polyurethane and ZIF-8 in a polymer-MOF nanocomposite: Microstructural, thermo-mechanical and viscoelastic effects. Polymer (Guildf). **97**, 31-43 (2016).
DOI: https://doi.org/10.1016/j.polymer.2016.05.012

[29] S. Shahid, K. Nijmeijer, S. Nehache, I. Vankelecom, A. Deratani, D. Quemener, MOF-mixed matrix membranes: Precise dispersion of MOF particles with better compatibility via a particle fusion approach for enhanced gas separation properties. J. Memb. Sci. **492**, 21-31 (2015).
DOI: https://doi.org/ 10.1016/j.memsci.2015.05.015

[30] E.M. Mahdi, J.C. Tan, Mixed-matrix membranes of zeolitic imidazolate framework (ZIF-8)/Matrimid nanocomposite: Thermo-mechanical stability and viscoelasticity underpinning membrane separation performance. J. Memb. Sci. **498**, 276-290 (2016).
DOI: https://doi.org/ 10.1016/j.memsci.2015.09.066

[31] Z. Wang, F. Liu, W. Liang, L. Zhou, Study on Tensile Properties of Nanoreinforced Epoxy Polyme : Macroscopic Experiments and Nanoscale FEM Simulation Prediction. **2013** (2017).

[32] A.M. Marti, S.R. Venna, E.A. Roth, J.T. Culp, D.P. Hopkinson, Simple Fabrication Method for Mixed Matrix Membranes with in Situ MOF Growth for Gas Separation. ACS Appl. Mater. Interfaces **10**, 29, 24784-24790 (2018).
DOI: https://doi.org/ 10.1021/acsami.8b06592